Coordinate-space solver for finite-temperature Hartree-Fock-Bogoliubov calculations using the shifted Krylov method

Yu Kashiwaba[1,*] and Takashi Nakatsukasa[2,1,3,†]

[1]*Faculty of Pure and Applied Sciences, University of Tsukuba, Tsukuba 305-8577, Japan*
[2]*Center for Computational Sciences, University of Tsukuba, Tsukuba 305-8577, Japan*
[3]*RIKEN Nishina Center, Wako 351-0198, Japan*

(Received 24 December 2019; accepted 26 March 2020; published 24 April 2020)

Background: In order to study structure of protoneutron stars and those in subsequent cooling stages, it is of great interest to calculate inhomogeneous hot and cold nuclear matter in a variety of phases. The finite-temperature Hartree-Fock-Bogoliubov (FT-HFB) theory is a primary choice for this purpose; however, its numerical calculation for superfluid (superconducting) many-fermion systems in three dimensions requires enormous computational costs.
Purpose: To study a variety of phases in the crust of hot and cold neutron stars, we propose an efficient method to perform the FT-HFB calculation with the three-dimensional (3D) coordinate-space representation.
Methods: Recently, an efficient method based on the contour integral of Green's function with the shifted conjugate-orthogonal conjugate-gradient method was proposed [Phys. Rev. C **95**, 044302 (2017)]. We extend the method to finite temperature, using the shifted conjugate-orthogonal conjugate-residual method.
Results: We benchmark the 3D coordinate-space solver of the FT-HFB calculation for hot isolated nuclei and fcc phase in the inner crust of neutron stars at finite temperature. The computational performance of the present method is demonstrated. Different critical temperatures of the quadrupole and the octupole deformations are confirmed for ^{146}Ba. The robustness of the shape coexistence feature in ^{184}Hg is examined. For the neutron-star crust, deformed neutron-rich Se nuclei embedded in the sea of superfluid low-density neutrons appear in the fcc phase at a nucleon density of 0.045 fm^{-3} and a temperature of $k_BT = 200$ keV.
Conclusions: The efficiency of the developed solver is demonstrated for nuclei and inhomogeneous nuclear matter at finite temperature. It may provide a standard tool for nuclear physics, especially for the structure of hot and cold neutron-star matter.

DOI: 10.1103/PhysRevC.101.045804

I. INTRODUCTION

The mean-field approaches, such as Hartree-Fock (HF) and Hartree-Fock-Bogoliubov (HFB) theories, have been playing a central role in studying heavy nuclei and nuclear matter [1]. They are especially useful for studies of ground (stationary) states. In addition, the time-dependent extension of the mean-field theories is straightforward and provides a powerful tool for studies of nuclear response and reaction [2–5]. Including the pairing correlations, a number of calculations have been performed with the BCS approximation [6–9]. Recently, studies of three-dimensional (3D) nuclear dynamics using the full time-dependent Hartree-Fock-Bogoliubov (TDHFB) method have become available [10–17]. The time evolution of the TDHFB states requires calculations of all the time-dependent quasiparticle states, which is computationally very demanding.

The static HFB calculation seems to be easier than the time-dependent problems, at first sight. However, in fact, it is often more difficult than the the time-dependent calculation. This is due to the requirement of the self-consistency between the HFB state and the HFB Hamiltonian. A standard procedure is as follows. The diagonalization of the HFB Hamiltonian produces the quasiparticle states. The quasiparticle states define the normal and pair densities which determine the HFB Hamiltonian. Iteration is necessary to reach the self-consistency. For the full 3D unrestricted calculations, finding a self-consistent solution is not as simple as it might seem. It involves successive diagonalization of matrices with large dimension N, which normally needs operations of $O(N^3)$. Most of available codes of the HFB calculation utilize some symmetry restriction on the densities, such as spatial symmetry and time-reversal symmetry, in order to reduce both the matrix dimension and the number of iterations [18–20]. The HFB program HFODD [21] is able to perform the unrestricted calculation; however, since it is based on the harmonic-oscillator basis, it is difficult to calculate nuclei near the neutron drip line and various phases of nuclear matter in neutron stars.

Recently, a novel computational approach to the HFB iterative problem was proposed by Jin, Bulgac, Roche, and Wlazłowski [22]. In contrast to the conventional methods,

*kashiwaba@nucl.ph.tsukuba.ac.jp
†nakatsukasa@nucl.ph.tsukuba.ac.jp

this approach has several favorable aspects, especially in large-scale calculations. (1) The densities are calculated by the contour integral in the complex energy plane, without quasiparticle wave functions. The matrix diagonalization is unnecessary. (2) It is based on the shifted Krylov subspace method for calculating the Green's function $G(\boldsymbol{r}, \boldsymbol{r}'; z)$ with complex energies z. The shifted method allows us to obtain simultaneously the Green's function with different energies z. (3) It is suited for parallel computing, because the Green's function $G(\boldsymbol{r}, \boldsymbol{r}'; z)$ is calculable independently for each point $\boldsymbol{r}'$. In Ref. [22], they explored the shifted conjugate-orthogonal conjugate-gradient (COCG) method, and showed a few benchmark calculations with the coordinate-space representation.

In this paper, we propose an extension of the 3D coordinate-space HFB method of Ref. [22] to that at finite temperature, namely the finite-temperature HFB (FT-HFB) calculation. The FT-HFB method is valuable for studying a variety of aspects in nuclear and many-fermion systems. For example, the structure and the composition of (proto)neutron stars depend on the equation of state (EOS) of baryonic matter at finite temperature. In order to calculate inhomogeneous baryonic matter in the crust region, the 3D coordinate-space FT-HFB solver is highly desired. For experimental studies on nuclear structure, giant dipole resonances in hot nuclei provide us information on nuclear shapes at finite temperature [23]. In order to study shape change together with pairing and shell quenching in hot nuclei, the FT-HFB is a valuable tool. The shape dynamics at finite temperature may play an important role in induced fission processes [24,25]. The FT-HFB method has also been utilized to study the level density [26,27], which is one of the key ingredients in the statistical reaction model.

The paper is organized as follows. In Sec. II, we recapitulate the FT-HFB theory, then we present a computational method of the contour integral to produce the normal and abnormal densities. It is slightly more complicated than the zero-temperature HFB method in Ref. [22], because we need to remove contributions from the Matsubara frequencies on the imaginary axis. In Sec. III, we demonstrate some numerical results. Finally, the summary and the perspectives are given in Sec. IV.

II. THEORETICAL FORMULATION

In this section, we first recapitulate the FT-HFB theory, then we introduce the Green's function method for that. Readers are referred to Ref. [22] for the zero-temperature formulation.

A. Finite-temperature HFB theory

Considering a system of spin-1/2 particles with the volume V and the Hamiltonian $\hat{H}$, in a thermal equilibrium with a heat bath of temperature T and chemical potential μ. The grand partition function is given by $Z(T, V, \mu) \equiv \mathrm{Tr}[e^{-\beta(\hat{H}-\mu\hat{N})}]$, where $\beta \equiv (k_B T)^{-1}$, and $\hat{N} \equiv \sum_\sigma \int_V \hat{\psi}^\dagger(\boldsymbol{r}\sigma)\hat{\psi}(\boldsymbol{r}\sigma)d\boldsymbol{r}$ is the particle number operator. In nuclear physics, we need to treat both protons and neutrons (isospin degrees of freedom). This extension can be easily done by incorporating both proton and neutron densities when we calculate potentials in Eq. (13).

The mean-field approximation replaces $\hat{H} - \mu\hat{N}$ by the HFB Hamiltonian which is given in terms of independent quasiparticles. Using the quasiparticle number operator $\hat{n}_k \equiv \hat{\gamma}_k^\dagger \hat{\gamma}_k$ with the creation and annihilation operators $(\hat{\gamma}_k^\dagger, \hat{\gamma}_k)$, The HFB Hamiltonian is simply written as

$$\hat{H}_{\mathrm{HFB}} = E_0 - \mu N_0 + \sum_{k>0} E_k \hat{n}_k, \tag{1}$$

where E_0 is the energy of the HFB ground state $|0\rangle$ with the particle number $N_0 = \langle 0|\hat{N}|0\rangle$, and $k > 0$ means the quasiparticle states with positive energies $E_k > 0$. The state $|0\rangle$ is defined as the quasiparticle vacuum.

$$\hat{\gamma}_k |0\rangle = 0 \quad \text{for } k > 0. \tag{2}$$

The trace in the partition function is calculated by summing up expectation values with respect to all the n-quasiparticle states with $n = 0, 1, \ldots$:

$$Z_{\mathrm{HFB}}(T, V, \mu) = e^{-\beta(E_0 - \mu N_0)} \prod_{k>0} (1 + e^{-\beta E_k}), \tag{3}$$

which leads to the density matrix

$$\hat{\rho}_{\mathrm{HFB}}(T, V, \mu) = \frac{e^{-\beta\hat{H}_{\mathrm{HFB}}}}{Z_{\mathrm{HFB}}(T, V, \mu)} = \frac{\prod_{k>0} e^{-\beta E_k \hat{n}_k}}{\prod_{k>0}(1 + e^{-\beta E_k})}. \tag{4}$$

Thus, the one-body densities are given as

$$\begin{aligned}\rho_T(\xi, \xi') &\equiv \mathrm{Tr}[\hat{\rho}_{\mathrm{HFB}} \hat{\psi}^\dagger(\xi')\hat{\psi}(\xi)] \\ &= \sum_{k>0} \{f_k u_k(\xi) u_k^*(\xi') + (1 - f_k) v_k^*(\xi) v_k(\xi')\}, \end{aligned} \tag{5}$$

$$\begin{aligned}\kappa_T(\xi, \xi') &\equiv \mathrm{Tr}[\hat{\rho}_{\mathrm{HFB}} \hat{\psi}(\xi')\hat{\psi}(\xi)] \\ &= \sum_{k>0} \{(1 - f_k) v_k^*(\xi) u_k(\xi') + f_k u_k(\xi) v_k^*(\xi')\}, \end{aligned} \tag{6}$$

where ξ indicates the coordinate and spin, $\xi = (\boldsymbol{r}, \sigma)$, and the quasiparticle occupation is given by

$$f_k \equiv \frac{1}{e^{\beta E_k} + 1}. \tag{7}$$

For Eqs. (5) and (6), we use the Bogoliubov transformation,

$$\hat{\psi}^\dagger(\xi) = \sum_{k>0} [u_k^*(\xi)\hat{\gamma}_k^\dagger + v_k(\xi)\hat{\gamma}_k], \tag{8}$$

$$\hat{\psi}(\xi) = \sum_{k>0} [u_k(\xi)\hat{\gamma}_k + v_k^*(\xi)\hat{\gamma}_k^\dagger]. \tag{9}$$

Using the matrix notation of

$$U_{\xi k} = u_k(\xi), \quad V_{\xi k} = v_k(\xi), \quad f_{kk'} = f_k \delta_{kk'}, \tag{10}$$

Eqs. (5) and (6) can be denoted in a compact form:

$$\begin{aligned}\rho_T &= U f U^\dagger + V^*(1 - f)V^T, \\ \kappa_T &= U f V^\dagger + V^*(1 - f)U^T. \end{aligned} \tag{11}$$

The quasiparticle energies and wave functions are obtained by solving the HFB equation

$$\begin{bmatrix} h & \Delta \\ -\Delta^* & -h^* \end{bmatrix} \begin{bmatrix} u_k \\ v_k \end{bmatrix} = E_k \begin{bmatrix} u_k \\ v_k \end{bmatrix}, \tag{12}$$

where $h(\xi,\xi')$ and $\Delta(\xi,\xi')$ are formally given by the derivatives of the energy density functional (EDF) $\mathcal{E}[\rho,\kappa]$,

$$h(\xi,\xi') = \frac{\delta\mathcal{E}}{\delta\rho(\xi',\xi)} - \mu\delta(\xi,\xi'),$$
$$\Delta(\xi,\xi') = \frac{\delta\mathcal{E}}{\delta\kappa^*(\xi,\xi')}. \tag{13}$$

Here, we use a simplified notation $\delta(\xi,\xi') \equiv \delta(\boldsymbol{r}-\boldsymbol{r}')\delta_{\sigma\sigma'}$.

B. HFB Hamiltonian for Skyrme EDF

In the Skyrme functional, the nuclear energy is written as $E[\rho,\kappa] = \int d\boldsymbol{r}\mathcal{E}(\boldsymbol{r})$, where the energy density is given by the sum of kinetic, nuclear potential, Coulomb, and pairing energies:

$$\mathcal{E} = \mathcal{E}_{\rm kin} + \mathcal{E}_{\rm nuclear} + \mathcal{E}_{\rm Coul} + \mathcal{E}_{\rm pair}. \tag{14}$$

The energy density is a functional of local densities, such as normal density $\rho_q(\boldsymbol{r})$, kinetic density $\tau_q(\boldsymbol{r})$, spin-current density $\boldsymbol{J}_q(\boldsymbol{r})$, and the pair (abnormal) density $\nu_q(\boldsymbol{r})$, with $q = n$ and p. These densities are calculated from the one-body densities, Eqs. (5) and (6). The energy density of the Coulomb exchange is given by the Slater approximation,

$$\mathcal{E}_{\rm Coul}(\boldsymbol{r}) = \frac{e^2}{2}\int\frac{\rho_p(\boldsymbol{r})\rho_p(\boldsymbol{r}')}{|\boldsymbol{r}-\boldsymbol{r}'|}d\boldsymbol{r}' - \frac{3e^2}{4}\left(\frac{3}{\pi}\right)^{1/3}\rho_p^{4/3}(\boldsymbol{r}). \tag{15}$$

The pairing energy density depends on the local pairing density,

$$\mathcal{E}_{\rm pair}(\boldsymbol{r}) = \sum_{q=n,p} g_{\rm eff}(\boldsymbol{r})|\nu_q(\boldsymbol{r})|^2, \tag{16}$$

where the effective pairing strength $g_{\rm eff}$ is determined via a renormalization [28] of the bare pairing strength g_0. The adopted value for g_0 in the present paper is given in Sec. III. The local nature of the Skyrme energy density leads to the HFB equation (12) in the coordinate representation of the form

$$H_{\rm HFB}\begin{pmatrix}u_{k\uparrow}\\ u_{k\downarrow}\\ v_{k\uparrow}\\ v_{k\downarrow}\end{pmatrix} = E_k\begin{pmatrix}u_{k\uparrow}\\ u_{k\downarrow}\\ v_{k\uparrow}\\ v_{k\downarrow}\end{pmatrix}, \tag{17}$$

$$H_{\rm HFB} = \begin{pmatrix} h_{\uparrow\uparrow} & h_{\uparrow\downarrow} & 0 & \Delta \\ h_{\downarrow\uparrow} & h_{\downarrow\downarrow} & -\Delta & 0 \\ 0 & -\Delta^* & -h^*_{\uparrow\uparrow} & -h^*_{\uparrow\downarrow} \\ \Delta^* & 0 & -h^*_{\downarrow\uparrow} & -h^*_{\downarrow\downarrow} \end{pmatrix}. \tag{18}$$

Here and hereafter in this section, the isospin index $q = n, p$ is omitted for simplicity. $h_{\sigma\sigma'} \equiv h(\xi,\xi')$ of Eq. (13) with $\xi = (\boldsymbol{r}\sigma)$ and $\xi' = (\boldsymbol{r}'\sigma')$, which are diagonal in the coordinate except for the derivative terms. Δ is strictly diagonal, $\Delta(\boldsymbol{r},\boldsymbol{r}') = \Delta(\boldsymbol{r})\delta(\boldsymbol{r}-\boldsymbol{r}')$ with

$$\Delta(\boldsymbol{r}) = g_{\rm eff}(\boldsymbol{r})\nu(\boldsymbol{r}). \tag{19}$$

All the local densities are calculable from the one-body densities, (5) and (6), at temperature T:

$$\rho(\boldsymbol{r}) = \sum_\sigma \rho_T(\boldsymbol{r}\sigma,\boldsymbol{r}\sigma), \tag{20}$$
$$\nu(\boldsymbol{r}) = \kappa_T(\boldsymbol{r}\uparrow,\boldsymbol{r}\downarrow), \tag{21}$$
$$\tau(\boldsymbol{r}) = \sum_\sigma \boldsymbol{\nabla}_1\cdot\boldsymbol{\nabla}_2\rho_T(\boldsymbol{r}\sigma,\boldsymbol{r}\sigma), \tag{22}$$
$$\boldsymbol{J}(\boldsymbol{r}) = \frac{1}{2i}(\boldsymbol{\nabla}_1-\boldsymbol{\nabla}_2)\times\boldsymbol{s}(\boldsymbol{r},\boldsymbol{r}) \tag{23}$$

where $\boldsymbol{\nabla}_{1(2)}$ indicates the differentiation on the first (second) argument $\boldsymbol{r}$ of the densities. Here, the spin density $\boldsymbol{s}(\boldsymbol{r},\boldsymbol{r}')$ is defined in terms of the Pauli matrix $\boldsymbol{\sigma}$ as

$$\boldsymbol{s}(\boldsymbol{r},\boldsymbol{r}') = \sum_{\sigma\sigma'}\rho_T(\boldsymbol{r}\sigma,\boldsymbol{r}'\sigma')\langle\sigma'|\boldsymbol{\sigma}|\sigma\rangle. \tag{24}$$

In the present paper, we assume time-reversal symmetry. We use the following relations to reduce the computational cost:

$$\rho_T(\boldsymbol{r}\sigma,\boldsymbol{r}'\sigma') = s_\sigma s_{\sigma'}\rho^*_T(\boldsymbol{r}\bar\sigma,\boldsymbol{r}'\bar\sigma'), \tag{25}$$
$$\kappa_T(\boldsymbol{r}\sigma,\boldsymbol{r}'\sigma') = s_\sigma s_{\sigma'}\kappa^*_T(\boldsymbol{r}\bar\sigma,\boldsymbol{r}'\bar\sigma'), \tag{26}$$

where $\bar\sigma = (\downarrow,\uparrow)$ for $\sigma = (\uparrow,\downarrow)$, and $s_\uparrow = -s_\downarrow = 1$. Thus, we need to calculate only those with $\sigma' = \uparrow$. All the time-odd densities vanish.

C. Green's functions and local densities

Now, let us present a method using the Green's function to calculate the local densities at finite temperature. The Green's functions of the HFB equation (17),

$$G(z) = \begin{pmatrix} G_{uu}(z;\xi,\xi') & G_{uv}(z;\xi,\xi') \\ G_{vu}(z;\xi,\xi') & G_{vv}(z;\xi,\xi')\end{pmatrix}, \tag{27}$$

are defined by a solution of

$$(zI - H_{\rm HFB})G(z) = I, \tag{28}$$

with a proper boundary condition. Here, I is the unit matrix. Each element of Eq. (27) can be expressed as

$$\begin{aligned}
G_{uu}(z;\xi;\xi') &= \sum_{k>0}\left[\frac{u_k(\xi)u_k^*(\xi')}{z-E_k} + \frac{v_k^*(\xi)v_k(\xi')}{z+E_k}\right],\\
G_{uv}(z;\xi,\xi') &= \sum_{k>0}\left[\frac{u_k(\xi)v_k^*(\xi')}{z-E_k} + \frac{v_k^*(\xi)u_k(\xi')}{z+E_k}\right],\\
G_{vu}(z;\xi,\xi') &= \sum_{k>0}\left[\frac{v_k(\xi)u_k^*(\xi')}{z-E_k} + \frac{u_k^*(\xi)v_k(\xi')}{z+E_k}\right],\\
G_{vv}(z;\xi,\xi') &= \sum_{k>0}\left[\frac{v_k(\xi)v_k^*(\xi')}{z-E_k} + \frac{u_k^*(\xi)u_k(\xi')}{z+E_k}\right].
\end{aligned} \tag{29}$$

For zero temperature, the densities are given by Eq. (11) with $f_{kk'} = f_k\delta_{kk'} = 0$, namely, $\rho_0 = V^*V^T$ and $\kappa_0 = V^*U^T$. Consider a contour C_1 that encloses the section $[-E_{\rm cut}, -E_1]$ on the real axis, and C_2 that does the section $[E_1, E_{\rm cut}]$, where $E_1 > 0$ is the lowest quasiparticle energy and $E_{\rm cut}$ is the cutoff energy of the pairing model space. It is easy to find from

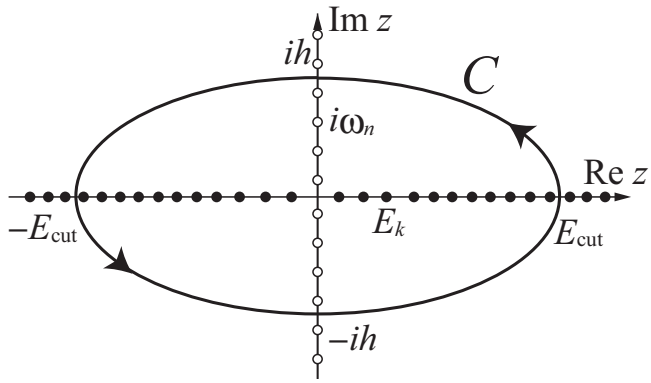

FIG. 1. Schematic illustration of the contour C and poles of the Green's function $G(z)$ (closed circles) and of the Fermi-Dirac function $f_T(z)$ (open circles) in the complex plane.

Eq. (29) that the generalized density matrix $R_0 = R_{T=0}$ can be calculated as

$$\frac{1}{2\pi i}\int_{C_1} G(z)dz = \begin{pmatrix} \rho_0 & \kappa_0 \\ -\kappa_0^* & 1-\rho_0^* \end{pmatrix} \equiv R_{T=0}, \tag{30}$$

$$\frac{1}{2\pi i}\int_{C_2} G(z)dz = \begin{pmatrix} 1-\rho_0 & -\kappa_0 \\ \kappa_0^* & \rho_0^* \end{pmatrix} = I - R_{T=0}. \tag{31}$$

Utilizing this property, the authors in Ref. [22] proposed a coordinate-space solver of the HFB calculation.

1. *Finite temperature and Matsubara frequencies*

The idea to extend this formulation to finite temperature is formally straightforward. Using the Fermi-Dirac distribution function $f_T(z) \equiv (1+e^{\beta z})^{-1}$,

$$\frac{1}{2\pi i}\oint_{C_1+C_2} f_T(z)G(z)dz = R_T, \tag{32}$$

$$\frac{1}{2\pi i}\oint_{C_1+C_2} f_T(-z)G(z)dz = I - R_T, \tag{33}$$

where we assume that the contour C_1 (C_2) is confined in the left (right) half-plane of $\mathrm{Re}(z) < 0$ [$\mathrm{Re}(z) > 0$]. Note that $f_T(-z) = 1 - f_T(z)$. Equations (32) and (33) are formally correct; however, they are not so useful in actual numerical calculations. Since we do not know the lowest quasiparticle energy E_1, we must adopt the contours, C_1 and C_2, passing through the origin $z = 0$. The Fermi-Dirac function $f_T(z)$ has poles at the Matsubara frequencies $z = i\omega_n = i(2n+1)\pi/\beta$ with the integer $n \gtrless 0$. At lower temperature ($\beta \to \infty$), the Matsubara poles are closer to the origin, and the numerical integration becomes more demanding.

The integrands in Eqs. (32) and (33) are smooth functions far away from the real axis. Even near the Matsubara frequencies on the imaginary axis, the absolute value is reduced as $1/z$. Therefore, numerically, the contour integration is easier with a contour further away from the real axis. We consider here the contour C that encloses the section $[-E_{\mathrm{cut}}, E_{\mathrm{cut}}]$ on the real axis and $[-ih, ih]$ on the imaginary axis. See Fig. 1. Since the function $f_T(\pm z)$ has residues $\mp\beta^{-1}$ at $z = i\omega_n$, we have

$$R_T = \frac{1}{2\pi i}\oint_C f_T(z)G(z)dz + \frac{1}{\beta}\sum_{|\omega_n|<h} G(i\omega_n), \tag{34}$$

$$I - R_T = \frac{1}{2\pi i}\oint_C f_T(-z)G(z)dz - \frac{1}{\beta}\sum_{|\omega_n|<h} G(i\omega_n). \tag{35}$$

The sum of these leads to an identity for the Green's function,

$$\frac{1}{2\pi i}\oint_C G(z)dz = I. \tag{36}$$

According to Eqs. (34) and (35), the normal and pair densities are calculated in various ways. Since we parallelized the computation with respect to the second argument ξ', each processor can calculate column vectors of Eq. (27) with fixed ξ'. For instance, from Eq. (35),

$$\rho_T^*(\xi,\xi') = \frac{1}{2\pi i}\oint_C \frac{G_{vv}(z;\xi,\xi')}{1+\exp(-\beta z)}dz - k_BT\sum_{|\omega_n|<h} G_{vv}(i\omega_n;\xi,\xi'), \tag{37}$$

$$-\kappa_T(\xi,\xi') = \frac{1}{2\pi i}\oint_C \frac{G_{uv}(z;\xi,\xi')}{1+\exp(-\beta z)}dz - k_BT\sum_{|\omega_n|<h} G_{uv}(i\omega_n;\xi,\xi'), \tag{38}$$

with

$$\omega_n = \pm\pi k_BT, \pm 3\pi k_BT, \pm 5\pi k_BT, \ldots . \tag{39}$$

The densities, Eqs. (37) and (38), can be obtained from the solution of the linear equations (28) without finding wave functions $(u_k(\xi), v_k(\xi))$. We parametrize the contour C as an ellipse of

$$z(\theta) = E_{\mathrm{cut}}\cos\theta + ih\sin\theta, \tag{40}$$

where $0 \leqslant \theta \leqslant 2\pi$ and the height of ellipse h is chosen as the midpoint of two neighboring Matsubara frequencies,

$$h = 2m\pi/\beta, \quad m = \text{integer}. \tag{41}$$

In practice, the contour integral is performed by dividing C into four intervals, $(0, \pi/2)$, $(\pi/2, \pi)$, $(\pi, 3\pi/2)$, and $(3\pi/2, 2\pi)$. We adopt the Gauss-Legendre integration for each of these intervals. The value of the integrand rapidly changes near the end points of these intervals, $\phi = 0, \pi/2, \pi, 3\pi/2, 2\pi$, where the number of the Gauss-Legendre integral points increases.

It is instructive to consider the limit of $T \to 0$. In this limit, the Fermi-Dirac function $f_T(z)$ is nothing but a step function, $\theta(-\mathrm{Re}(z))$. It vanishes in the half-plane of $\mathrm{Re}(z) > 0$, while it is unity in the other half-plane of $\mathrm{Re}(z) < 0$. Thus, in the first term of Eq. (34), the integrand can be replaced by $G(z)$, then the closed contour C can be changed into the open one ($\pi/2 < \theta < 3\pi/2$) for $\mathrm{Re}(z) < 0$ and terminated on the imaginary axis at $z = \pm ih$. It is known that the summation with respect to the Matsubara frequencies becomes the integration of the Green's function on the imaginary axis at

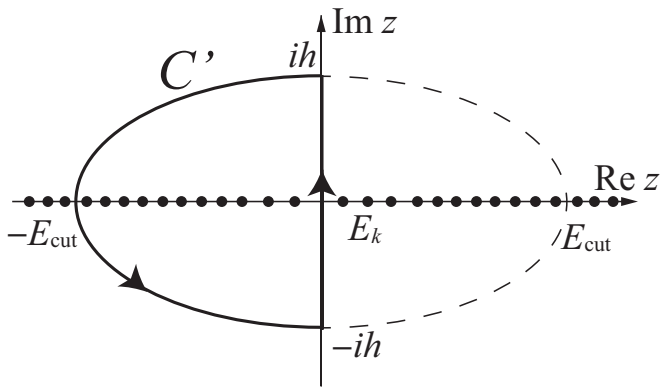

FIG. 2. Schematic illustration of the contour C' and poles of the Green's function $G(z)$ (closed circles).

$T \to 0$. So, the second term of Eq. (34) becomes

$$\frac{1}{2\pi i}\sum_{|\omega_n|<h} G(i\omega_n)\frac{2\pi i}{\beta} \to \frac{1}{2\pi i}\int_{-ih}^{ih} G(z)dz, \quad \beta \to \infty. \tag{42}$$

Therefore, Eq. (34) at the zero-temperature limit is identical to

$$R_T = \frac{1}{2\pi i}\int_{C'} G(z)dz, \tag{43}$$

where the contour C is shown in Fig. 2. In this way, we recover the zero-temperature formula, (30). Following the same argument, it is easy to obtain Eq. (31) from the zero-temperature limit of Eq. (35).

2. Kinetic and spin-current densities in parallel computing

The numerical calculation is parallelized by allocating the calculation of densities $\rho_T(\xi,\xi')$ and $\kappa_T(\xi,\xi')$ with different $\boldsymbol{r}'$ of the second argument $\xi' = (\boldsymbol{r}', \sigma')$ on different processors. Therefore, it is useful to eliminate the derivative ∇_2 in expressions of Eqs. (22) and (23). The calculation of the spin-current density $\boldsymbol{J}(\boldsymbol{r})$ is done by

$$J_x(\boldsymbol{r}) = -\,\mathrm{Im}\left[\frac{\partial}{\partial y_1}\rho_T^*(\boldsymbol{r}\uparrow;\boldsymbol{r}\uparrow) - \frac{\partial}{\partial y_1}\rho_T^*(\boldsymbol{r}\downarrow;\boldsymbol{r}\downarrow)\right] + \mathrm{Re}\left[\frac{\partial}{\partial z_1}\rho_T^*(\boldsymbol{r}\downarrow;\boldsymbol{r}\uparrow) - \frac{\partial}{\partial z_1}\rho_T^*(\boldsymbol{r}\uparrow;\boldsymbol{r}\downarrow)\right], \tag{44}$$

$$J_y(\boldsymbol{r}) = \mathrm{Im}\left[\frac{\partial}{\partial x_1}\rho_T^*(\boldsymbol{r}\uparrow;\boldsymbol{r}\uparrow) - \frac{\partial}{\partial x_1}\rho_T^*(\boldsymbol{r}\downarrow;\boldsymbol{r}\downarrow)\right] - \mathrm{Im}\left[\frac{\partial}{\partial z_1}\rho_T^*(\boldsymbol{r}\downarrow;\boldsymbol{r}\uparrow) + \frac{\partial}{\partial z_1}\rho_T^*(\boldsymbol{r}\uparrow;\boldsymbol{r}\downarrow)\right], \tag{45}$$

$$J_z(\boldsymbol{r}) = \mathrm{Im}\left[\frac{\partial}{\partial y_1}\rho_T^*(\boldsymbol{r}\downarrow;\boldsymbol{r}\uparrow) + \frac{\partial}{\partial y_1}\rho_T^*(\boldsymbol{r}\uparrow;\boldsymbol{r}\downarrow)\right] - \mathrm{Re}\left[\frac{\partial}{\partial x_1}\rho_T^*(\boldsymbol{r}\downarrow;\boldsymbol{r}\uparrow) - \frac{\partial}{\partial x_1}\rho_T^*(\boldsymbol{r}\uparrow;\boldsymbol{r}\downarrow)\right]. \tag{46}$$

The densities of Eqs. (20), (21), and (23) at $\boldsymbol{r} = \boldsymbol{r}'$ can be computed by each processor without any communication. The local densities necessary for construction of the HFB Hamiltonian, $\rho(\boldsymbol{r})$, $\nu(\boldsymbol{r})$, and $\boldsymbol{J}(\boldsymbol{r})$, are obtained locally ($\boldsymbol{r} = \boldsymbol{r}'$) at each processor then broadcast to all the processors. The kinetic density of Eq. (22) is calculated according to

$$\tau(\boldsymbol{r}) = \frac{1}{2}\nabla^2\rho(\boldsymbol{r}) - \mathrm{Re}\sum_\sigma \nabla_1^2\rho_T(\boldsymbol{r}\sigma;\boldsymbol{r}\sigma). \tag{47}$$

Here, every processor calculates the Laplacian in the first term after broadcasting $\rho(\boldsymbol{r})$, then constructs an updated HFB Hamiltonian.

D. Shifted-COCR method

In numerical calculations, the most computationally demanding parts are solutions of the linear equations (28). This is suitable for massively parallel computing, because Eq. (28) can be solved independently for different values of $\boldsymbol{r}'$ in the calculation of $G(z;\xi,\xi')$.

Another advantageous feature of Eq. (28) is that the shifted Krylov subspace method is applicable to these linear equations, in which a family of the linear algebraic equations (28) for different values of z are solved simultaneously. For the numerical integration in Eqs. (34) or (35), we need to solve Eq. (28) with many values of z, at discretized contour points z_m ($m = 0, 1, \ldots, M$). In Ref. [22], the shifted conjugate-orthogonal conjugate-gradient (COCG) method [29] is adopted. In this paper, we use a similar but different algorithm, the shifted conjugate-orthogonal conjugate-residual (COCR) method [30]. The COCG method is an efficient method for positive-definite symmetric matrices. In the present case, the Hamiltonian $H_{\rm HFB}$ is clearly not positive definite, and we have found that the COCR method is more stable than the COCG method for our purpose. Here, we briefly present the algorithm of the shifted-COCR method.

Given a symmetric matrix A, we solve the reference equation

$$A\boldsymbol{x} = \boldsymbol{b}, \tag{48}$$

and shifted equations

$$(A + \sigma I)\boldsymbol{x}^\sigma = \boldsymbol{b}, \tag{49}$$

where σ is a complex scalar factor. In the present case, σ is nothing but z. Note that, hereafter, the superscript σ indicates merely the index, not the power σ. The reference equation (48) is solved by the COCR method. An approximate solution $\boldsymbol{x}_{k+1}$ and its residual vector $\boldsymbol{r}_{k+1}$ in the $(k+1)$th iteration are calculated according to the following iterative algorithm:

$$\alpha_k = (A\boldsymbol{r}_k, \boldsymbol{r}_k)/(A\boldsymbol{p}_k, A\boldsymbol{p}_k), \tag{50}$$

$$\boldsymbol{x}_{k+1} = \boldsymbol{x}_k + \alpha_k\boldsymbol{p}_k, \tag{51}$$

$$\boldsymbol{r}_{k+1} = \boldsymbol{r}_k - \alpha_k A\boldsymbol{p}_k, \tag{52}$$

$$\beta_k = (A\boldsymbol{r}_{k+1}, \boldsymbol{r}_{k+1})/(A\boldsymbol{r}_k, \boldsymbol{r}_k), \tag{53}$$

$$\boldsymbol{p}_{k+1} = \boldsymbol{r}_{k+1} + \beta_k\boldsymbol{p}_k, \tag{54}$$

$$A\boldsymbol{p}_{k+1} = A\boldsymbol{r}_{k+1} + \beta_k A\boldsymbol{p}_k, \tag{55}$$

with the initial conditions $\boldsymbol{x}_0 = 0, \boldsymbol{r}_0 = \boldsymbol{b}, \alpha_0 = 1, \beta_0 = 0$. Here, the inner product $(\boldsymbol{v}, \boldsymbol{v}')$ is defined by a scalar product $\boldsymbol{v}^T \cdot \boldsymbol{v}'$ without complex conjugation. The matrix-vector oper-

ation is necessary only for evaluating $A\boldsymbol{r}_k$, which is the most time-consuming part in this iteration.

We can also solve shifted equations (49) using the COCR method with the same initial condition as the reference system. However the residual vectors in shifted systems have a linear relation with the reference system,

$$\boldsymbol{r}_k^\sigma = \rho_k^\sigma \boldsymbol{r}_k, \tag{56}$$

$$\rho_{k+1}^\sigma = \frac{\rho_k^\sigma \rho_{k-1}^\sigma \alpha_{k-1}}{\rho_{k-1}^\sigma \alpha_{k-1}(1+\alpha_k\sigma) + \alpha_k\beta_{k-1}\left(\rho_{k-1}^\sigma - \rho_k^\sigma\right)}. \tag{57}$$

with the initial conditions $\rho_0^\sigma = 1$. This linear relation reduces the computational cost from $O(N^2M)$ to $O(N^2+NM)$, where N is the dimension of the matrix A and M is the number of complex shifts σ, because we can avoid the time-consuming calculation of the matrix-vector product $A\boldsymbol{r}_k^\sigma$. The coefficients, α_k^σ and β_k^σ, are also obtained from those of the reference system. Thus, for the shifted systems, we simply perform the following calculations:

$$\alpha_k^\sigma = \frac{\rho_{k+1}^\sigma}{\rho_k^\sigma}\alpha_k, \tag{58}$$

$$\beta_k^\sigma = \left(\frac{\rho_{k+1}^\sigma}{\rho_k^\sigma}\right)^2 \beta_k, \tag{59}$$

$$\boldsymbol{x}_{k+1}^\sigma = \boldsymbol{x}_k^\sigma + \alpha_k^\sigma \boldsymbol{p}_k^\sigma, \tag{60}$$

$$\boldsymbol{p}_{k+1}^\sigma = \boldsymbol{r}_k^\sigma - \alpha_k^\sigma \boldsymbol{p}_k^\sigma. \tag{61}$$

The iterations for the reference and the shifted systems are performed simultaneously.

In practice, it is unnecessary to calculate all the elements of $\boldsymbol{x}_k^\sigma$ and $\boldsymbol{p}_k^\sigma$ for the shifted systems ($\sigma \neq 0$), because wanted physical quantities are often sparse in the coordinate space. For instance, any quantity local in the coordinate requires us to calculate only one component for each $\boldsymbol{r}'$. This is similar to the reduced-shifted-COCG method proposed in Ref. [31].

The COCR method is designed for a symmetric matrix A, but the HFB Hamiltonian is a Hermitian matrix, in general. Following Ref. [22], we also transform linear Hermitian problems into real symmetric ones. Dividing a Hermitian matrix A into real and imaginary parts, the equation $A\boldsymbol{x} = \boldsymbol{b}$ can be converted into

$$\begin{pmatrix} \mathrm{Re}[A] & -\mathrm{Im}[A] \\ \mathrm{Im}[A] & \mathrm{Re}[A] \end{pmatrix} \begin{pmatrix} \mathrm{Re}[\boldsymbol{x}] \\ \mathrm{Im}[\boldsymbol{x}] \end{pmatrix} = \begin{pmatrix} \mathrm{Re}[\boldsymbol{b}] \\ \mathrm{Im}[\boldsymbol{b}] \end{pmatrix}. \tag{62}$$

Because ReA (ImA) is symmetric (antisymmetric), the matrix in Eq. (62) is a real symmetric matrix. The shifted systems with complex scalar shifts σ are defined as

$$\begin{pmatrix} \sigma I + \mathrm{Re}[A] & -\mathrm{Im}[A] \\ \mathrm{Im}[A] & \sigma I + \mathrm{Re}[A] \end{pmatrix} \begin{pmatrix} \boldsymbol{x}_1 \\ \boldsymbol{x}_2 \end{pmatrix} = \begin{pmatrix} \mathrm{Re}[\boldsymbol{b}] \\ \mathrm{Im}[\boldsymbol{b}] \end{pmatrix}, \tag{63}$$

where $\boldsymbol{x}_1$ and $\boldsymbol{x}_2$ are no longer real but complex vectors, namely, $(\boldsymbol{x}_1, \boldsymbol{x}_2) \neq (\mathrm{Re}[\boldsymbol{x}], \mathrm{Im}[\boldsymbol{x}])$. Nevertheless, the solution of the original problem $(\sigma I + A)\boldsymbol{x} = \boldsymbol{b}$ is constructed by the relation $\boldsymbol{x} = \boldsymbol{x}_1 + i\boldsymbol{x}_2$.

The performance of the shifted-COCR method will be shown in Sec. III B. In practice, it is not necessary to obtain a full convergence of the shifted-COCR method with all the complex shifts σ, because what we need is the accurate estimation of the densities, ρ and κ, by the contour integration, Eqs. (37) and (38). Therefore, we calculate the densities every 100 iterations, and estimate the difference between the "old" and the "new" densities, $\delta\rho \equiv \rho^{(\mathrm{new})} - \rho^{(\mathrm{old})}$ and $\delta\nu \equiv \nu^{(\mathrm{new})} - \nu^{(\mathrm{old})}$. Then, the convergence condition is set as follows:

$$|\delta\rho(\boldsymbol{r}'\uparrow)| < \epsilon_1, \quad |\delta\nu(\boldsymbol{r}'))| < \epsilon_1', \tag{64}$$

$$\left|\frac{\delta\rho(\boldsymbol{r}'\uparrow)}{\rho^{(\mathrm{old})}(\boldsymbol{r}'\uparrow)}\right| < \epsilon_2, \quad \left|\frac{\delta\nu(\boldsymbol{r}')}{\nu^{(\mathrm{old})}(\boldsymbol{r}')}\right| < \epsilon_2', \tag{65}$$

with $\epsilon_1 = 10^{-8}$ fm^{-3}, $\epsilon_1' = 10^{-6}$ fm^{-3}, and $\epsilon_2 = \epsilon_2' = 10^{-6}$. We stop the COCR iteration when either Eq. (64) or (65) is satisfied.

E. Self-consistent solutions

The iterative calculation is performed according to the following procedure.

(1) Input the initial densities and chemical potentials, $V^{(i)} = \{\rho^{(i)}(\boldsymbol{r}), \nu^{(i)}(\boldsymbol{r}), \tau^{(i)}(\boldsymbol{r}), \boldsymbol{J}^{(i)}(\boldsymbol{r}), \mu_q^{(i)}\}$ $(i = 0)$.
(2) Calculate the HFB Hamiltonian, $h_{\sigma\sigma'}(\boldsymbol{r})$ and $\Delta_q(\boldsymbol{r})$, and the total energy $E^{(i)}$.
(3) Solve the shifted linear equations (28) to determine the Green's functions $G(z)$.
(4) Calculate the contour integrals of Eqs. (37) and (38) to determine the densities and the chemical potentials, $V_{\mathrm{out}}^{(i)}$. The updated chemical potential is given by $(\mu_q)_{\mathrm{out}}^{(i)} = \mu_q^{(i)} + \alpha_0 \tanh[\alpha_1/\alpha_0(\langle N_q\rangle - N_q)]$.
(5) Calculate the energy E_{out}. If the convergence condition, $|E_{\mathrm{out}} - E_{\mathrm{in}}^{(i)}| < \eta$, is satisfied, the iteration stops.
(6) Determine the new densities and chemical potentials using the modified Broyden mixing, $V^{(i+1)} = V^{(i)} + \sum_{j=i-n}^{i} w_j[V_{\mathrm{out}}^{(j)} - V^{(j)}]$. Go back to Step 2.

In Step 4, α_0 and α_1 are the parameters to ensure convergence, whose typical values are $\alpha_0 = 5$ and $\alpha_1 = 0.1$–1.0. In Step 5, the parameter η is taken as $\eta = 10^{-5} \times A$ MeV for finite nuclei (Secs. III C and III D) and $\eta = 10^{-6} \times A$ MeV for the inner crust of neutron stars (Sec. III E), where A is the number of nucleons. In Step 6, w_j are obtained by the modified Broyden method [32]. We store the densities and the chemical potentials of the last n iterations for the Broyden mixing, with $n = 10$.

III. NUMERICAL RESULTS

We present a few benchmark results of the FT-HFB calculation in this paper, with some numerical details and its computational performance. In the following calculations, the Skyrme energy density functional of SLy4 [33] is adopted. The pairing energy functional is in the form of Eq. (16) with the bare pairing strength $g_0 = -250\,\mathrm{MeV\,fm}^3$. This pairing energy functional well reproduces the two-neutron separation energies for Sn and Pb isotopes [34]. We adopt either a square or a rectangular box with a square mesh, and impose a periodic boundary condition.

A. Symmetry restriction

We have constructed a computer program of the full 3D coordinate-space representation. This is used for the FT-HFB calculation for ^{146}Ba in Sec. III C. However, in order to speed up the calculation, reflection symmetry with respect to the three planes $x = 0$, $y = 0$, and $z = 0$ is assumed in the calculations in Secs. III D and III E.

In the conventional calculation of the quasiparticle wave functions, to be benefited by this restriction, we need to take care of symmetry properties of the wave functions. Each of the three types of reflection produces eigenvalues (quantum numbers) of $\pi_k = \pm 1$ $(k = x, y, z)$ for the wave functions. Therefore, the HFB Hamiltonian is block diagonal into eight blocks, which means that the dimension of each block is $1/8$ of the full 3D Hamiltonian matrix. The coordinate space can be also reduced into the first octant $(x > 0, y > 0, z > 0)$ however, we need to impose a proper symmetry on the wave functions of each block: $(\pi_x, \pi_y, \pi_z) = (+++), (++-), ..., (---)$.

In contrast, the symmetry restriction can be treated much more easily in the present Green's function method, because we do not calculate the quasiparticle wave functions. The Hamiltonian is invariant with respect to the three reflections. Therefore, the Hamiltonian in the first octant can be simply copied to the other spatial regions. Then, Eq. (28) is solved only for $G(z; \xi, \xi')$ with $\boldsymbol{r}'$ in the first octant. This reduces the computational cost to $1/8$ of the full calculation. Here, we do not need to take care of different symmetry properties of the wave functions, according to their quantum numbers.

B. Performance of shifted-COCR method

In this paper, we adopt the shifted-COCR method for the solution of the linear algebraic equations (28). In contrast, the shifted-COCG method was adopted for the zero-temperature HFB calculation in Ref. [22]. First, let us show differences in their convergence behavior.

In Fig. 3, we show an example of convergence properties. The HFB Hamiltonian $H_{\rm HFB}$ at the converged solution is used for showing performance of the shifted-COCR and the shifted-COCG methods to solve Eq. (28). The pure imaginary shift of $z = ih = 16\pi i k_B T$ $(\theta = \pi/2)$ with the COCR method shows the fastest convergence. The convergence behavior at $z = 0$ best demonstrates superiority of the COCR method over the COCG. The convergence with the COCR is faster by about 1000 iterations than the COCG. Moreover, it indicates a monotonic decrease of the residue, while the COCG shows a strong oscillating behavior. In general, we may expect that the convergence is slower when the shift z is closer to the pole of the integrand. In this respect, $z = E_{\rm cut}$ represents the worst case. In fact, Fig. 3 shows that the solution at $z = E_{\rm cut} = 100$ MeV $(\theta = 0)$ fails to converge within 4000 iterations in both the COCG and COCR methods, and the residue $|\boldsymbol{r}_n^\sigma/\boldsymbol{r}_0^\sigma|$ keeps oscillating between 10^{-2} and 1. This is not a serious problem in the calculation, because the quasiparticle states with $E_k \approx E_{\rm cut}$ hardly contribute to the densities. In addition, moving z away from the real axis, the convergence property is quickly improved.

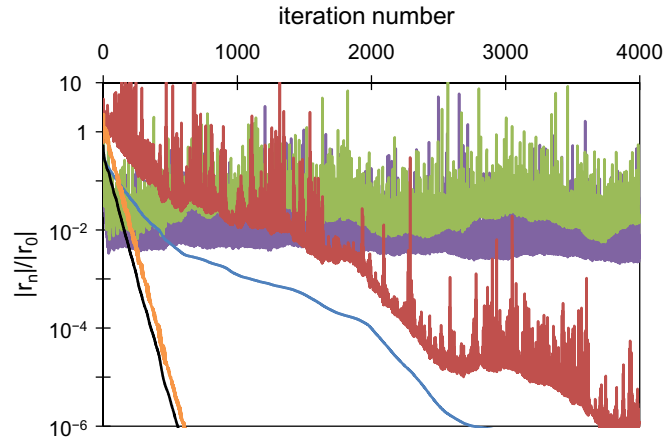

FIG. 3. The convergence behavior of the shifted-COCG and shifted-COCR methods for solutions of Eq. (28). Three typical points, $z(\theta = 0)$ (COCG/COCR: purple/green) and $z(\pi/2)$ (orange/black) on the contour of Eq. (40) with $E_{\rm cut} = 100$ MeV and $h = 16\pi k_B T$, in addition to the reference point $z = 0$ (red/blue), have been taken as examples. The norms of the residual vectors $|\boldsymbol{r}_k^\sigma/\boldsymbol{r}_0^\sigma|$ are shown as functions of the iteration number. This is a case of the FT-HFB calculation for the center of mass of a ^{146}Ba nucleus $(\boldsymbol{r}' = \boldsymbol{r}_c)$ with a temperature of $k_B T = 200$ keV. The mesh and box sizes are the same as those in Sec. III C.

We calculate the normal and pair densities, $\rho(\boldsymbol{r}\uparrow)$ and $\nu(\boldsymbol{r})$, using the Green's function $G(z)$ at each iteration before the convergence. In Fig. 4, we show the densities as functions of the iteration number for the COCG and COCR methods. Note that the HFB Hamiltonian $H_{\rm HFB}$ is not updated during the iteration. The densities are well converged after a few hundred iterations in the scale of Fig. 4. Again, the convergence is faster and more stable with the COCR method than with the COCG. Even though the shifted-COCR/COCG methods fail to converge at z very near $E_{\rm cut}$, the densities constructed by the contour integrals, Eqs. (37) and (38), can be accurately estimated. To achieve the convergence condition of Eq. (64), typically about 3000 iterations are required.

In order to reach the final self-consistent solution, another self-consistent iteration is necessary. In Sec. II E, we present the iterative procedure with the Broyden mixing to obtain the self-consistent solutions. This self-consistent iteration requires about several tens to hundreds of iterations.

Finally, let us give short comments on comparisons with other typical approaches to the HFB problem. The standard approach to the HFB calculation is based on the diagonalization of the HFB matrix (see Sec. I). This approach becomes more and more difficult for larger systems without the symmetry restriction, because the diagonalization of matrices with dimension N requires a computational task of $O(N^3)$. The comparison with the shifted-COCG method $(T = 0)$ is shown in Ref. [22]. The performance of the present shifted-COCR method at $T \neq 0$ should be similar to that of the shifted-COCG at $T = 0$. Another well-known approach to the HFB calculation is the gradient method [35–37]. The gradient method does not require the diagonalization of the HFB matrix; however, it directly treats the wave functions

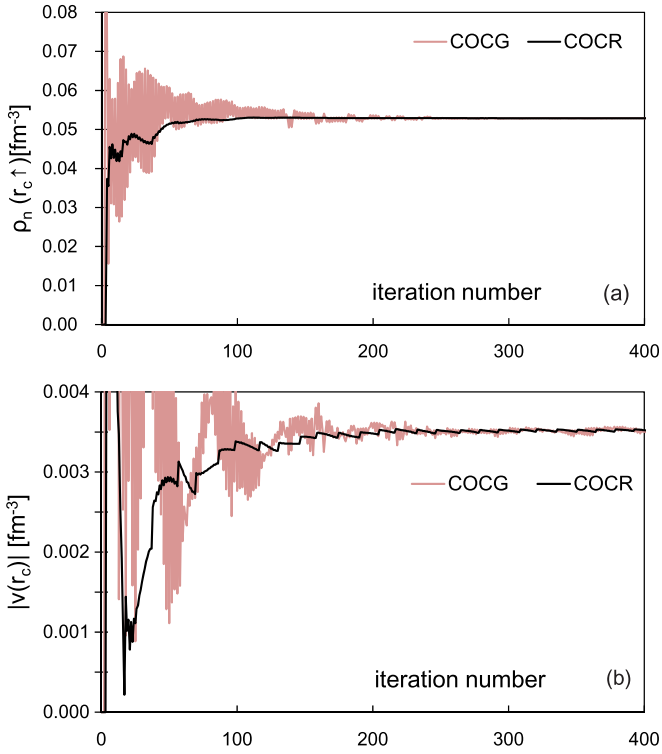

FIG. 4. The convergence behavior of (a) the neutron spin-up density $\rho(\boldsymbol{r}'\uparrow,\boldsymbol{r}'\uparrow)$ and (b) the neutron pair density $\nu(\boldsymbol{r}') = \kappa(\boldsymbol{r}'\uparrow, \boldsymbol{r}'\downarrow)$ at the center of mass of a ^{146}Ba nucleus ($\boldsymbol{r}' = \boldsymbol{r}_c$) with k_BT = 200 keV. The shifted-COCG method is shown by red lines and the shifted-COCR method by black lines. See text for details.

(u_k, v_k) which are basically $N \times N$ matrices. Therefore, in parallel computing, it involves a large amount of communication to broadcast these to all the processors. Furthermore, the orthonormalization of the wave functions is necessary, which numerically costs $O(N^3)$. The present shifted-COCR method needs the broadcast of local densities ("vectors," not "matrices") only, and does not require the orthonormalization procedure since we do not treat the wave functions. See also Sec. II C 2.

C. Octupole deformation in ^{146}Ba at finite temperature

We perform the FT-HFB calculation for the neutron-rich nucleus ^{146}Ba as the first benchmark calculation. A full 3D box of lattice size 25 × 25 × 30 with a square mesh of $\Delta x = \Delta y = \Delta z = 1$ fm is used in the calculation. The calculations are performed with a temperature spacing of $k_BT = 100$ keV.

The nucleus of ^{146}Ba has $Z = 56$ and $N = 90$, which is in a region of strong octupole correlations [38]. The excitation energies of negative-parity states decrease as the neutron number approaches to 90, and a signature of the octupole instability, alternating parity bands, was observed in experiments at spins higher than $I = 6$ [39,40]. This is due to particle-hole octupole correlations associated with $\pi[h_{11/2}(d_{5/2})^{-1}]$ and $\nu[i_{13/2}(f_{7/2})^{-1}]$. Thus, we may expect an octupole deformed shape in the ground state of the zero-temperature HFB theory

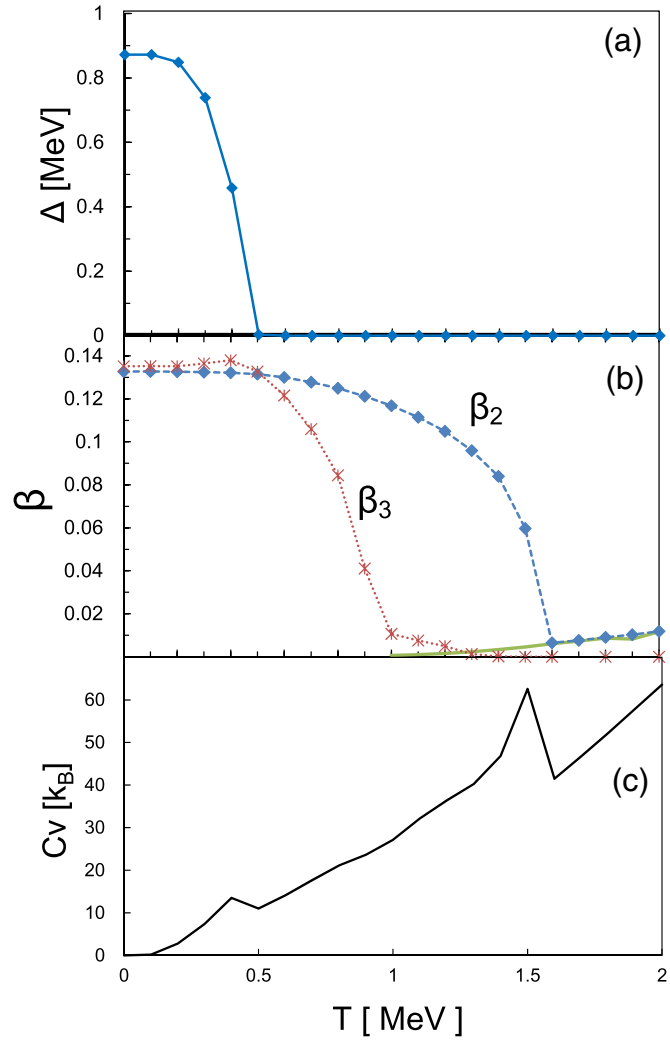

FIG. 5. (a) Calculated neutron average paring gap, (b) quadrupole and octupole deformation parameters, and (c) specific heat as functions of temperature for ^{146}Ba. In panel (b), the quadrupole deformation of the dripped uniform neutrons is shown by the solid line.

[41] and it is interesting to see effects of finite temperature on its structure.

The proton pair density is calculated to vanish. We show the neutron average pairing gap in Fig. 5(a). The neutron gap is finite at low temperature but disappears at k_BT = 500 keV. In this calculation, the transition from super to normal phases for neutrons is predicted at $400 < k_BT \leqslant 500$ keV. In contrast, the nuclear deformation is more stable against the temperature. At the ground state (zero temperature), the calculation predicts finite values for both quadrupole and octupole deformations, $\beta_2 \approx \beta_3 \approx 0.13$. Figure 5(b) shows the temperature dependence of these deformation parameters. At $k_BT = 500$ keV, where the neutron pairing collapses, the temperature effects on β_2 and β_3 are very little. They are almost identical to their values at $T = 0$. Beyond k_BT = 500 keV, the octupole deformation starts decreasing and becomes negligibly small at $k_BT > 1$ MeV. The quadrupole deformation is even more robust but suddenly vanishes at

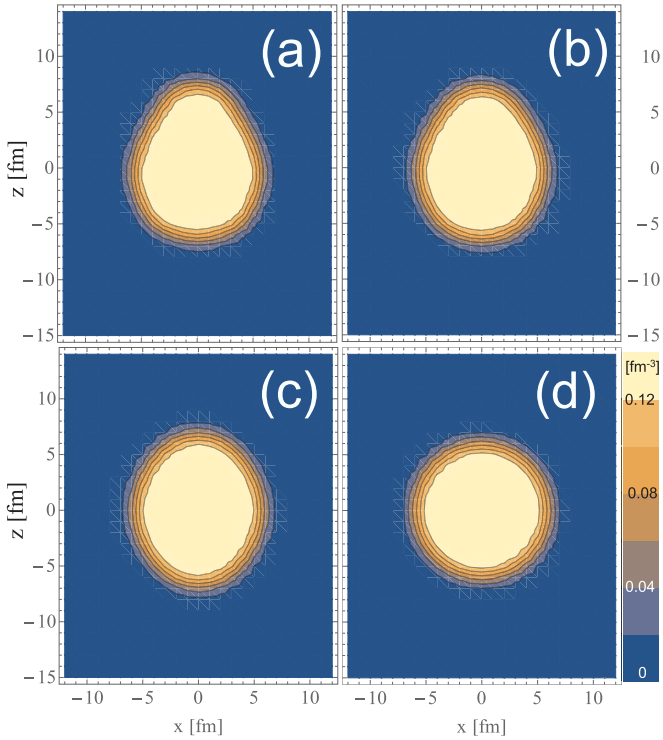

FIG. 6. Nucleon density profiles in the z-x plane for ^{146}Ba at different temperatures: (a) $T = 0$, (b) $k_BT = 0.8$ MeV, (c) $k_BT = 1.2$ MeV, and (d) $k_BT = 1.6$ MeV.

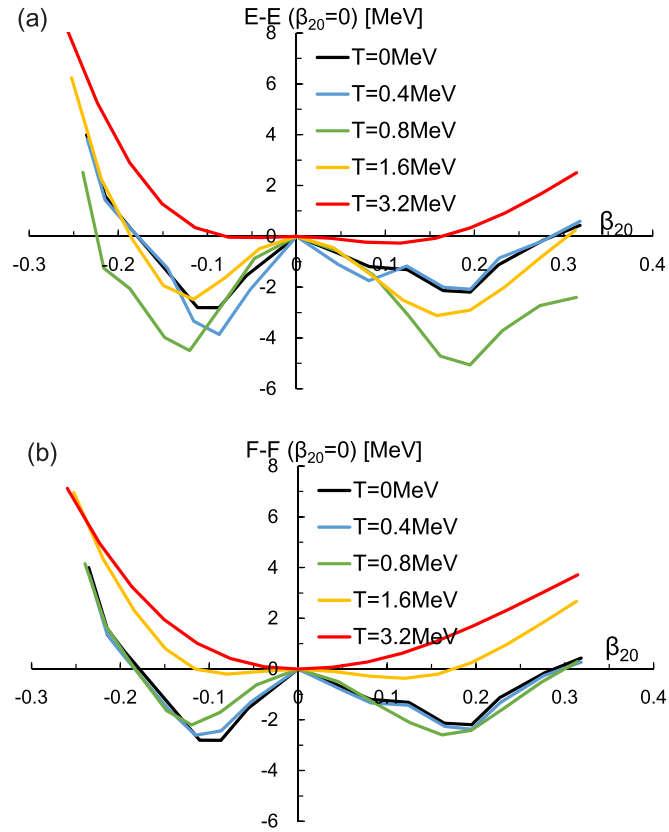

FIG. 7. Potential energy surface, calculated with the constrained FT-HFB method, as a function of the quadrupole deformation, for ^{184}Hg. Panel (a) is the total energy E, while panel (b) is the free energy F. See text for details.

$k_BT = 1.6$ MeV. At temperature between 1 and 1.6 MeV, the nuclear shape is almost prolate. Beyond $k_BT = 1.6$ MeV, the shape becomes spherical. These shape changes can be clearly seen in the density distributions in Fig. 6.

The quadrupole deformation is finite and slightly increases with temperature at $k_BT > 1.6$ MeV. This is due to effects of dripped neutrons at finite temperature. Because of the adopted rectangular box, the dripped "free" neutrons form a rectangular shape which has a nonzero value of β_2. To confirm this, assuming a uniform density distribution of neutrons with calculated density values at the box boundary, we estimate the β_2 value which is shown by the solid line in Fig. 5(b).

Finally, the specific heat $C_V(T)$ is shown in Fig. 5(c). The specific heat is estimated by the finite difference of the total energies calculated at $k_BT \pm 0.01$ MeV. The calculated $C_V(T)$ is approximately a linear function of the temperature T, similar to that of the Fermi gas. However, at very low temperature $T \approx 0$, because of the proton shell gap and the neutron pairing gap, it deviates from linear dependence. In addition, we observe sudden decreases of $C_V(T)$ at special points of T, where abrupt changes in nuclear structure take place. The first drop is associated with the collapse of the neutron pairing at $k_BT \approx 500$ keV, while the second one is associated with the shape change from prolate to spherical at $k_BT \approx 1.6$ MeV. On the other hand, the disappearance of the octupole shape around $k_BT \approx 1$ MeV has very little influence on it. In contrast, the transition to the spherical shape ($k_BT \approx 1.6$ MeV) leads to a significant impact on the specific heat, a sudden decrease by more than 30 %. This may be due to an enhanced shell effect by the recovered spherical symmetry.

D. Shape coexistence in ^{184}Hg at finite temperature

The neutron-deficient Hg isotopes are known to be typical nuclei showing shape coexistence phenomena [42–44]. Much evidence of the shape coexistence has been observed, including coexisting bands with different deformation in even isotopes and anomalously large isotope shifts in odd-A isotopes. Note that the Hg isotopes also exhibit superdeformed bands at high spins [45] on which octupole vibrations are built [46].

We have studied the temperature effect on the shape coexistence with the FT-HFB calculation using a constraint on the quadrupole deformation β_{20}. A 3D box of lattice size 30^3 with a square mesh of $\Delta x = \Delta y = \Delta z = 1$ fm is adopted however, we assume reflection symmetry with respect to the three planes ($x = 0$, $y = 0$, and $z = 0$) and reduce the computational cost. The calculations are performed with different temperatures: $k_BT = 0$, 0.4, 0.8, 1.6, 3.2 MeV. A quadratic constraint on the deformation β_{20} is used with a spacing of $\Delta\beta_{20} = 0.04$.

Figure 7 shows the temperature dependence of the potential energy surface for ^{184}Hg. The total energy $E(\beta, T)$ is calculated at each deformation and temperature, then, the energy relative to the value at $\beta_{20} = 0$ is plotted in the panel (a), while the free energy $F(\beta, T)$ is shown in the panel (b). We

can clearly see two local minima at prolate and oblate shapes. At $T = 0$, the deformation and the pairing gaps at the oblate minimum are calculated as $\beta_{20} \approx -0.1$, $\Delta_n \approx 1.4$ MeV, and $\Delta_p = 0$. Those at the prolate minimum are $\beta_{20} \approx 0.2$, $\Delta_n \approx 0.8$ MeV, and $\Delta_p \approx 1$ MeV. The shape coexistence feature is quite robust against the finite temperature. Although the lowest minimum at zero temperature is in the oblate side, the prolate minima is more stable as increasing the temperature. The oblate minima are lower than the prolate ones at $k_BT \leqslant 400$ keV, while the prolate becomes lower at $k_BT \geqslant 800$ keV. The main features are the same for $E(\beta, T)$ and $F(\beta, T)$, except that a shallow prolate minimum exists for $E(\beta, T)$ but not for $F(\beta, T)$.

It is interesting to see that the nonzero temperature does not necessarily favor the spherical shape. The potential energy surfaces $E(\beta, T)$ at $k_BT = 0.8$ and 1.6 MeV indicate deeper prolate minima than that of zero temperature. This is also true for the free energy $F(\beta, T)$ at $k_BT = 0.8$. This may be partially due to the pairing collapse at finite temperature. For instance, at $k_BT = 0.8$ MeV, the proton pairing vanishes for all the values of deformation β_{20}. The neutron pairing gap still has nonzero values but only in the vicinity of the spherical shape ($\beta_{20} \approx 0$). The vanishing pairing may lead to stronger shell energy that favors the deformation.

We should note that the calculation of the free energy F requires an additional computation. In order to calculate $F \equiv E - TS$, we evaluate the entropy S using the formula

$$S = -k_B \sum_{k>0} [f_k \ln f_k + (1 - f_k) \ln(1 - f_k)], \qquad (66)$$

where f_k is given by Eq. (7) in which the quasiparticle energies E_k are defined as the eigenvalues of the constrained HFB Hamiltonian, namely, the mean-field approximation to $\hat{H} - \mu\hat{N} - \lambda\hat{Q}_{20}$. In the present Green's function method, since we do not explicitly calculate the quasiparticle states (and their energies), an additional diagonalization of the constrained HFB Hamiltonian is needed after the self-consistent iteration converges. We use the SCALAPACK library for this diagonalization.

E. Neutron-star inner crust at finite temperature

Neutron stars are a sort of macroscopic nucleus in the universe. They are assumed to be synthesized by explosive stellar phenomena, such as supernovae. Protoneutron stars are hot, but subsequently cool down to become cold neutron stars. It would be of great interest to study neutron star matter at a variety of temperatures, especially various inhomogeneous phases predicted to exist in the crust region near the surface.

Microscopic studies of the inner crust are theoretically very challenging, because the calculation requires a large space in which extremely neutron-rich nuclei and free neutrons coexist. In addition, the energy difference between different configurations is very small. Thus, to predict the structure of the inner crust, large-scale and highly accurate calculations are needed.

In this subsection, we present our first benchmark FT-HFB calculation for the inner crust. The full 3D box of $(45 \text{ fm})^3$ with a square mesh of $\Delta x = \Delta y = \Delta z = 1.5$ fm is reduced by 1/8 assuming reflection symmetry. The calculation is performed for a temperature of $k_BT = 200$ keV. We use an initial state for the iteration with the face-centered cubic(fcc) configuration. The adopted square box contains 4 nuclei. We fix the neutron chemical potential as $\mu_n = 10$ MeV, and determine the proton chemical potential μ_p to satisfy the beta equilibrium condition, $\mu_p + m_pc^2 + \mu_e = \mu_n + m_nc^2$, where the electrons are assumed to be uniform with the chemical potential $\mu_e = \sqrt{m_e^2c^4 + p_F^2c^2} - e^2(3n_e/\pi)^{1/3}$.

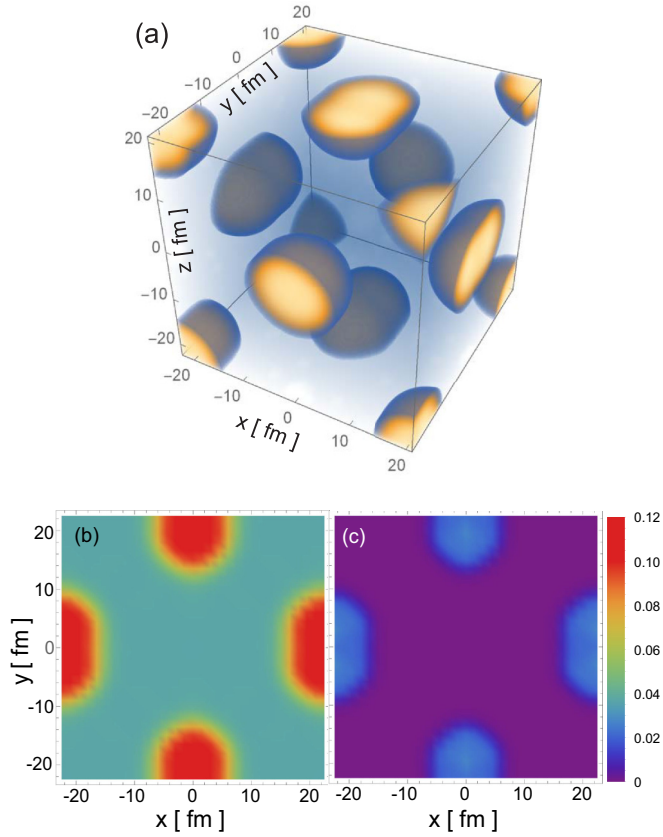

FIG. 8. Nucleonic density distribution in the inner crust of neutron stars at beta equilibrium with the neutron chemical potential $\mu_n = 10$ MeV and the proton chemical potential $\mu_p = -58.5$ MeV: (a) 3D plot of baryon density, (b) 2D contour plot of neutron density in the $z = 0$ plane, and (c) the same as (b) but for protons.

The self-consistent procedure converges to a fcc state shown in Fig. 8(a). The neutron and proton density distributions in the $z = 0$ plane are shown in Figs. 8(b) and 8(c), respectively. The protons are localized and form a fcc crystalline structure. The neutrons are dripped with a large number of free neutrons. The average nucleon density is 0.045 fm^{-3}, and the lowest neutron density between the nuclei is 0.036 fm^{-3}. The obtained average pairing gap for neutrons is 1.48 MeV and the proton gap vanishes. The proton and neutron numbers in the box shown in Fig. 8(a) are approximately 136 and 3936. Since the protons are all confined in the crust nuclei, we may say that emergent nuclei are very neutron-rich Se nuclei ($Z = 34$).

The most interesting feature we find in this result is that those Se nuclei are well deformed. This can be clearly seen

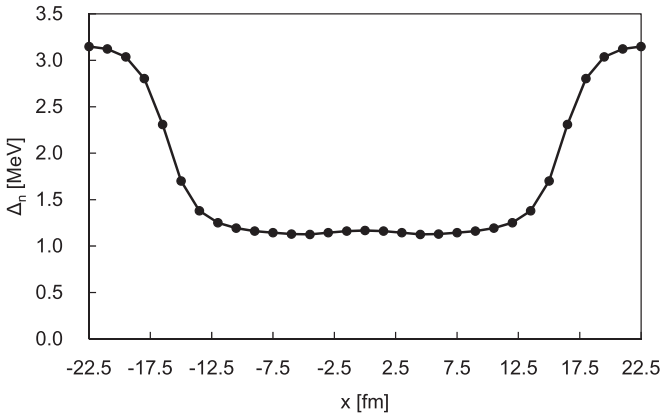

FIG. 9. Calculated neutron gap $\Delta_n(\boldsymbol{r})$ on the x axis. The protons are clustered near the both edges.

in the density distributions on the $z = 0$ plane shown in Figs. 8(b) and 8(c). They have prolate shape. We naively expect that, near the transition to the rod phase, elongated nuclei may appear, which is supported by the present microscopic calculation. This is certainly a self-consistent solution of the FT-HFB with the beta equilibrium at $k_BT = 200$ keV. However, we have not confirmed yet that this is really the optimal configuration at the given density. Further studies with various configurations, such as bcc and pasta phases, is necessary to find the structure of the inner crust.

In this state, the protons are in the normal phase, while the neutrons are in the superfluid phase. These superfluid neutrons are assumed to be responsible for pulsar glitches [47]. Figure 9 shows the neutron pairing gap $\Delta_n(\boldsymbol{r})$ on the x axis. The left and the right ends correspond to the center of the Se nuclei, while only dripped neutrons exist near the center ($x = 0$). The magnitude of the gap is about 1 MeV for dripped neutrons and even larger inside the nuclei. This is somewhat opposite to our naive expectation, since the pairing gap calculated with the bare force for uniform matter is larger at low density ($\rho_n < \rho_0 \approx 0.08$ fm^{-3}) than at high density ($\rho_n \gtrsim \rho_0$) [48,49]. However, it is premature to conclude the pairing property in the inner crust from this calculation. Since the present pairing energy functional is based on a simple zero-range interaction fitted to specific regions of finite nuclei [34], it is desirable to test the other functionals as well. Especially, the explicit density dependence of the coupling constant g_0 may be necessary for more realistic simulations [50,51].

IV. SUMMARY

We have developed the finite temperature Hartree-Fock-Bogoliubov (FT-HFB) method in the three-dimensional coordinate-space representation with the Green's function. This is an extension to finite temperature of the method proposed in Ref. [22]. In this method, neither quasiparticle wave functions nor the quasiparticle energies are necessary for the calculation. Thus, we can avoid the diagonalization of the HFB Hamiltonian. Various kinds of densities are evaluated by the contour integral in the complex energy plane. For the calculation of the Green's function with the complex energy, we have tested two different shifted Krylov methods: shifted-COCG and shifted-COCR methods. We find that the shifted-COCR methods are more stable and reach convergence faster. However, since the performance of the shifted-COCG and shifted-COCR may vary according to systems, energy functionals, space size, etc., we cannot conclude in this study that the COCR is always superior to the COCG. Further study is desired to find the best algorithm.

For the benchmark calculations, we showed the structure change in ^{146}Ba as a function of the temperature. The octupole deformation at the ground state disappears at $k_BT \approx 500$ keV, while the quadrupole deformation is much more stable and persists up to $k_BT \approx 1.6$ MeV. The effect of the shape transition to spherical is clearly visible in its specific heat.

The shape coexistence in ^{184}Hg is also studied with the FT-HFB calculation. It is somewhat surprising that the deformation minima become even deeper at finite temperature compared to those at zero temperature. The shape coexistence is quite robust with respect to the increasing temperature and seems to sustain up to $k_BT \approx 2$–3 MeV. The barrier height between prolate and oblate shapes is calculated to be more than 3 MeV, even at $k_BT = 1.6$ MeV.

The structure of inner crust of (hot and cold) neutron stars is a prime motivation of the present development [52]. The method has a significant advantage over the conventional methods for systems requiring such large spatial lattice sizes. For a benchmark, we have presented a beta-equilibrium fcc state at a nucleon density of 0.045 fm^{-3} and $k_BT = 200$ keV. Neutron-rich Se nuclei emerge and they are well deformed in the prolate shape. The transition from spherical to deformed nuclei is an interesting issue in the future study of the structure of the inner crust, as a function of density and temperature.

ACKNOWLEDGMENTS

This work is supported by JSPS KAKENHI Grants No. 18H01209 and No. 19H05142. We thank Y. Futamura and T. Sakurai for useful discussions on the shifted Krylov methods. This research used computational resources provided by the Joint Center for Advanced High Performance Computing (JCAHPC) through the HPCI System Research Project (Project ID hp190031) and through the Multidisciplinary Cooperative Research Program in Center for Computational Sciences, University of Tsukuba.

[1] M. Bender, P. H. Heenen, and P.-G. Reinhard, Rev. Mod. Phys. **75**, 121 (2003).
[2] T. Nakatsukasa, Prog. Theor. Exp. Phys. **2012**, 01A207 (2012).
[3] C. Simenel, Eur. Phys. J. A **48**, 152 (2012).
[4] A. Bulgac, Annu. Rev. Nucl. Part. Sci. **63**, 97 (2013).
[5] T. Nakatsukasa, K. Matsuyanagi, M. Matsuo, and K. Yabana, Rev. Mod. Phys. **88**, 045004 (2016).

[6] S. Ebata, T. Nakatsukasa, T. Inakura, K. Yoshida, Y. Hashimoto, and K. Yabana, Phys. Rev. C **82**, 034306 (2010).
[7] S. Ebata, T. Nakatsukasa, and T. Inakura, Phys. Rev. C **90**, 024303 (2014).
[8] G. Scamps and D. Lacroix, Phys. Rev. C **89**, 034314 (2014).
[9] G. Scamps, C. Simenel, and D. Lacroix, Phys. Rev. C **92**, 011602(R) (2015).
[10] I. Stetcu, A. Bulgac, P. Magierski, and K. J. Roche, Phys. Rev. C **84**, 051309 (2011).
[11] Y. Hashimoto, Eur. Phys. J. A **48**, 55 (2012).
[12] Y. Hashimoto, Phys. Rev. C **88**, 034307 (2013).
[13] I. Stetcu, C. A. Bertulani, A. Bulgac, P. Magierski, and K. J. Roche, Phys. Rev. Lett. **114**, 012701 (2015).
[14] Y. Hashimoto and G. Scamps, Phys. Rev. C **94**, 014610 (2016).
[15] P. Magierski, K. Sekizawa, and G. Wlazłowski, Phys. Rev. Lett. **119**, 042501 (2017).
[16] G. Scamps and Y. Hashimoto, Phys. Rev. C **96**, 031602(R) (2017).
[17] G. Scamps and Y. Hashimoto, Phys. Rev. C **100**, 024623 (2019).
[18] K. Bennaceur and J. Dobaczewski, Comput. Phys. Commun. **168**, 96 (2005).
[19] R. N. Perez, N. Schunck, R.-D. Lasseri, C. Zhang, and J. Sarich, Comput. Phys. Commun. **220**, 363 (2017).
[20] W. Ryssens, V. Hellemans, M. Bender, and P.-H. Heenen, Comput. Phys. Commun. **187**, 175 (2015).
[21] N. Schunck, J. Dobaczewski, W. Satuła, P. Bączyk, J. Dudek, Y. Gao, M. Konieczka, K. Sato, Y. Shi, X. Wang, and T. Werner, Comput. Phys. Commun. **216**, 145 (2017).
[22] S. Jin, A. Bulgac, K. Roche, and G. Wlazłowski, Phys. Rev. C **95**, 044302 (2017).
[23] A. Schiller and M. Thoennessen, At. Data Nucl. Data Tables **93**, 549 (2007).
[24] J. C. Pei, W. Nazarewicz, J. A. Sheikh, and A. K. Kerman, Phys. Rev. Lett. **102**, 192501 (2009).
[25] J. A. Sheikh, W. Nazarewicz, and J. C. Pei, Phys. Rev. C **80**, 011302(R) (2009).
[26] S. Hilaire, M. Girod, S. Goriely, and A. J. Koning, Phys. Rev. C **86**, 064317 (2012).
[27] N. Furutachi, F. Minato, and O. Iwamoto, J. Nucl. Sci. Technol. **56**, 412 (2019).
[28] A. Bulgac and Y. Yu, Phys. Rev. Lett. **88**, 042504 (2002).
[29] H. A. van der Vorst and J. B. M. Melissen, IEEE Trans. Magn. **26**, 706 (1990).
[30] T. Sogabe and S.-L. Zhang, East Asian J. Appl. Math. **1**, 97 (2011).
[31] Y. Nagai, Y. Shinohara, Y. Futamura, and T. Sakurai, J. Phys. Soc. Jpn. **86**, 014708 (2017).
[32] A. Baran, A. Bulgac, M. M. Forbes, G. Hagen, W. Nazarewicz, N. Schunck, and M. V. Stoitsov, Phys. Rev. C **78**, 014318 (2008).
[33] E. Chabanat, P. Bonche, P. Haensel, J. Meyer, and R. Schaeffer, Nucl. Phys. A **627**, 710 (1997).
[34] Y. Yu and A. Bulgac, Phys. Rev. Lett. **90**, 222501 (2003).
[35] P. Ring and P. Schuck, *The Nuclear Many-Body Problems*, Texts and Monographs in Physics (Springer, New York, 1980).
[36] J. Egido, J. Lessing, V. Martin, and L. Robledo, Nucl. Phys. A **594**, 70 (1995).
[37] L. M. Robledo and G. F. Bertsch, Phys. Rev. C **84**, 014312 (2011).
[38] P. A. Butler and W. Nazarewicz, Rev. Mod. Phys. **68**, 349 (1996).
[39] W. R. Phillips, I. Ahmad, H. Emling, R. Holzmann, R. V. F. Janssens, T. L. Khoo, and M. W. Drigert, Phys. Rev. Lett. **57**, 3257 (1986).
[40] S. Zhu, Q. Lu, J. Hamilton, A. Ramayya, L. Peker, M. Wang, W. Ma, B. Babu, T. Ginter, J. Kormicki, D. Shi, J. Deng, W. Nazarewicz, J. Rasmussen, M. Stoyer, S. Chu, K. Gregorich, M. Mohar, S. Asztalos, S. Prussin, J. Cole, R. Aryaeinejad, Y. Dardenne, M. Drigert, K. Moody, R. Loughed, J. Wild, N. Johnson, I. Lee, F. McGowan, G. Ter-Akopian, and Y. Oganessian, Phys. Lett. B **357**, 273 (1995).
[41] S. Ebata and T. Nakatsukasa, Phys. Scr. **92**, 064005 (2017).
[42] K. Heyde, P. V. Isacker, M. Waroquier, J. L. Wood, and R. A. Meyer, Phys. Rep. **102**, 291 (1983).
[43] J. L. Wood, K. Heyde, W. Nazarewicz, M. Huyse, and P. van Duppen, Phys. Rep. **215**, 101 (1992).
[44] K. Heyde and J. L. Wood, Rev. Mod. Phys. **83**, 1467 (2011).
[45] R. V. F. Janssens and T. L. Khoo, Annu. Rev. Nucl. Part. Sci. **41**, 321 (1991).
[46] T. Nakatsukasa, K. Matsuyanagi, S. Mizutori, and Y. R. Shimizu, Phys. Rev. C **53**, 2213 (1996).
[47] P. W. Anderson and N. Itoh, Nature (London) **256**, 25 (1975).
[48] T. Takatsuka and R. Tamagaki, Prog. Theor. Phys. Suppl. **112**, 27 (1993).
[49] D. J. Dean and M. Hjorth-Jensen, Rev. Mod. Phys. **75**, 607 (2003).
[50] M. Matsuo, Phys. Rev. C **73**, 044309 (2006).
[51] G. Wlazłowski, K. Sekizawa, P. Magierski, A. Bulgac, and M. M. Forbes, Phys. Rev. Lett. **117**, 232701 (2016).
[52] Y. Kashiwaba and T. Nakatsukasa, Phys. Rev. C **100**, 035804 (2019).